

Biomedical Image Registration by Means of Bacterial Foraging Paradigm

H. Costin, S. Bejinariu, D. Costin

Hariton Costin

¹Faculty of Medical Bioengineering Grigore T. Popa University of Medicine and Pharmacy, Iași, Romania

²Institute of Computer Science of Romanian Academy Iași Branch, Romania
hncostin@mail.umfiasi.ro

Silviu Bejinariu

²Institute of Computer Science of Romanian Academy Iași Branch, Romania
silviu.bejinariu@iit.academiaromana-is.ro

Diana Costin*

³Faculty of Medicine, Grigore T. Popa University of Medicine and Pharmacy, Iași, Romania

*Corresponding author: diana.costin@umfiasi.ro

Abstract: Image registration (IR) is the process of geometric overlaying or alignment of two or more 2D/3D images of the same scene (unimodal registration), taken or not at different time slots, from different angles, and/or by different image acquisition systems (multimodal registration). Technically, image registration implies a complex optimization of different parameters, performed at local or/and global level. Local optimization methods often fail because functions of the involved metrics with respect to transformation parameters are generally nonconvex and irregular, and global methods are required, at least at the beginning of the procedure. This paper presents a new evolutionary and bio-inspired robust approach for IR, Bacterial Foraging Optimization Algorithm (BFOA), which is adapted for PET-CT multimodal and magnetic resonance image rigid registration. Results of optimizing the normalized mutual information and normalized cross correlation similarity metrics validated the efficacy and precision of the proposed method by using a freely available medical image database.

Keywords: medical imaging, image registration, soft computing, evolutionary strategies, bacterial foraging algorithm, global optimization.

1 About Multimodal Image Registration

Image registration (IR) is a fundamental task in computer vision used to find either a spatial *transformation* (e.g., rotation, translation, etc.) or a correspondence (matching of similar image entities) among two (or more) images taken under different conditions (at different times, using different sensors, from different viewpoints, or a combination of them), with the aim of overlaying such images into a common one [1], [2], [3], [4]. Over the years, IR has been applied to a broad range of situations from remote sensing to medical images or artificial vision and CAD systems, and different techniques have been independently studied resulting in a large body of research.

IR methods can be classified in two groups according to the nature of images: *pixel/voxel*-based IR methods (also called *intensity*-based), where the whole image is considered for the registration process; and, on the other side, *feature*-based methods, which consider prominent information extracted from the images, being a reduced subset of them. The latter methods take advantage of the lesser amount of information managed in order to overcome the problems found in the former when the images present some inconsistencies to deal with, for example,

regardless of changes in the geometry of the images, radiometric conditions, and appearance of noise and occlusion. These features correspond to *geometric primitives* (points, lines, surfaces, etc.) which are invariant to the transformation to be considered between the input images. Moreover, the latter methods perform faster than the former ones due to the reduced amount of data they take into account, at the expense of achieving *coarse* results. Likewise, IR is the process of finding the optimal spatial transformation (e.g., rigid, similarity, affine, etc.) achieving the best overlaying between two (or more) different images named *scene and model images* (Figure 1). They both are related with the specific transformation, measured by a *similarity metric function*. Such transformation estimation is interpreted into an iterative optimization procedure in order to properly explore the search space. Two search approaches have been considered in the IR literature: *matching-based*, where the optimization problem is intended to look for a set of correspondences of pairs of those more similar image entities in both the scene and the model images, from which the registration transformation is derived; and the *transformation parameter-based*, where the strategy is to directly explore inside each range of the transformation parameters. Both strategies can be used with either a voxel-based or a feature-based approach.

Specific aspects such as the presence of noise, image discretization, different amplitudes in the scale of the IR transformation parameters, the magnitude of the transformation to be estimated cause difficulties for traditional local optimizers (gradient- and nongradient-based) and they become prone to be trapped in local minima. As a consequence, global methods are preferred, at least at the beginning of the IR process. As for image segmentation procedure, there is not a universal design for an IR method that could be applicable to all registration tasks, since various considerations on the particular application must be taken into account.

In recent years a lot of studies and papers were dedicated to medical IR, with more or less good results [5], [6], [7], [8], [9], [10], [11], [12], [13], [14], [15], [16], [15], [16], [17]. Thus, e.g. rigid 3D transformations were performed, e.g., by Alpert [18] using the images principal axes and center of gravity. Affine registration was obtained by Wahl [21], employing user identified anatomical landmarks and external markers, and Maguire et al. [22], who optimized cross-correlation around such user identified anatomical landmarks and external markers. In [11] a robust surface registration using a Gaussian-weighted distance map (GWDM) for PET-CT brain fusion was proposed. A similarity measure was evaluated repeatedly by weighted cross-correlation (WCC).

1.1 Transformations

The IR methods can also be classified according to the registration transformation used to relate both the scene and the model images. The first category of transformation models includes *linear transformations*, which preserves the operations of vector addition and scalar multiplication, being a combination of translation, rotation, global scaling, and shear components. The most common linear transformations are rigid, similarity, affine, projective, and curved. Linear transformations are global in nature, thus not being able to model local deformations. The second category of transformation models includes *elastic* and *nonrigid* transformations, which allow local warping of image features, thus providing support for local deformations.

1.2 Similarity Metric

The similarity metric is a function F that measures the goodness of a given registration solution, that is, of a registration transformation f . The final performance of any IR method strongly depends on its accurate estimation. Each solution is evaluated by F applying such transformation f on one of the two images, usually to the scene image ($f(I_s)$). Next, the degree of closeness or fitting between the transformed scene and the model images, $\Psi(\cdot)$ must be determined

$$F(I_s, I_m, f) = \Psi(f(I_s), I_m) \quad (1)$$

The main approaches trying to estimate the function $\Psi(\cdot)$ depend on the dimensionality (2D or 3D) and the nature of the considered images. There are: (a) voxel-based approach: sum of squared differences, normalized cross-correlation (i.e., correlation coefficient or phase correlation), and mutual information; (b) feature-based approach: feature values-based metrics (i.e., registration based on the curvature) and distance between corresponding geometric primitives.

Unfortunately, the F function is affected by both the discretization of images and the presence of noise, yielding worse estimations and favoring the IR to get trapped in local minima.

1.3 Search Space Strategies

The IR process performs an iterative exploration to obtain that optimal transformation f . So, the closer f to the unknown global optimum, the better the fitting (measured by the similarity metric F) between scene and model. The optimization process considered to obtain those solutions can be deterministic or stochastic (either a global or a local one).

Although the final registration problem solution consists of the right values for the parameters which determine f , we can distinguish two different strategies to solve the problem, each of them working in a different solution space: (i) the first searches in the *matching space* to obtain a set of correspondences of pairs of the most similar image entities in both the scene and the model images, from which the registration transformation is derived; (ii) the second directly makes a search in the space of the f parameters guided by the F function, called *transformation parameters space*. The matching-based search space exploration usually consists of the two following stages: first, a set of correspondences with those more similar regions of pixels (voxel-based) or geometric primitives (feature-based) in both the scene and the model images must be computed; second, the transformation f is assessed by numerical methods considering the previous matching.

On the contrary, transformation parameters-based search space involves directly searching for the solution in the space of parameters of the transformation f . In this respect, each solution to the IR problem is encoded as a vector composed of the values for the parameters of f , and the IR method generates possible vectors of parameter values, that is, possible registration transformations. As a consequence, the search space exploration is guided by the similarity metric F . In this way, each solution vector is evaluated by the chosen metric, and the IR problem becomes a parameter optimization procedure of finding the best values of f that maximize the similarity metric F . Other classification divides search strategies in *local* and *global* ones. Local optimization techniques frequently fail because functions of these metrics with respect to transformation parameters are generally nonconvex and irregular and, therefore, global methods – such as those based on evolutionary algorithms – are often required.

2 Optimization using BFOA

In recent years, the application of several well-known *evolutionary algorithms (EAs)* [23] to the IR optimization process has introduced an outstanding interest in order to solve those

problems due to their global optimization techniques nature. The first attempts to solve IR using evolutionary computation can be found in the early eighties, when Fitzpatrick et al. [24] proposed such approach based on a genetic algorithm for the 2D case and applied it to angiographic images. Since then, several evolutionary approaches have been proposed to solve the IR problem, mainly in connection with the transformation parameters-based search space, as shown e.g. in [25], [1], [26], [27], [28], [29], [30]. The main reason of using global optimization techniques, such as EAs-based algorithms for IR, is that they may not require an optimum solution to achieve high accuracy of registration.

Introduced by Passino [31], [32], bacterial foraging paradigm is a bio-inspired optimization method based on the foraging model. This paradigm belongs to the broader class of distributed nongradient global optimization. A foraging animal takes actions to maximize the energy obtained per unit time spent foraging, E/T , in the face of constraints presented by its own physiology (e.g., sensing and cognitive capabilities) and environment (e.g., density of prey, risks from predators, physical characteristics of the search area). In other words, these social animals, like *E. coli* – a bacterium, try to maximize their long-term average rate of energy intake.

Prominent applications in medical image processing are related to edge detection [33], image segmentation [19], [20], but also for image registration [36], [37], knowing that these procedures may be viewed as optimization tasks.

2.1 BFO Algorithm

The bacterial foraging paradigm is suitable as model for optimization algorithms because animals/bacteria behavior is to search for nutrients and avoid noxious substances to maximize their energy. As in all evolutionary models, individuals with a good strategy to find nutrients are replicated and those having poor foraging strategy are eliminated. In contrast to genetic algorithms and evolutionary strategies, which exploit the competitive characteristics of biological evolution (e.g., survival of the fittest), bacterial foraging (BF) exploits cooperative and social aspects of animal colonies (like *E. coli* bacterium) in their attempts to obtain nutrients that maximizes energy intake per unit time spent for foraging.

Each member of the bacteria colony is characterized by its position in the n -dimensional space which is a possible solution of the optimization problem. The solution is computed as the position in which a bacterium is in the best healthy state or has the lowest cost value. During foraging, the bacteria colony (swarm) proceeds through four foraging steps: chemotaxis, swarming, reproduction and elimination-dispersal.

Let's consider a bacteria colony with S individuals; $P(j, k, l) = \{\theta^t(j, k, l), i = 1 \dots S\}$ is the position of colony members in the j^{th} chemotactic step, k^{th} is the k -th reproduction step and l^{th} – the l -th elimination-dispersal step; $J(i, j, k, l)$ denotes the cost of the i^{th} bacterium in position $\theta^t(j, k, l)$.

- *Chemotaxis*: *E. Coli* bacteria have two types of movements: tumble and swim. The chemotactic step is defined as a tumble followed by a tumble or a tumble followed by a run. In the chemotactic step each bacterium changes its position to: $\theta^t(j + 1, k, l) = \theta^t(j, k, l) + C(i)\varphi(i)$, where $C(i)$ is the size of the chemotactic step and is a unit length random generated direction [4]. If the cost computed in the new position is lower than in the previous position, then the swim is continued in the same direction as long as the cost is reduced but not more than a maximum number of steps.
- *Swarming*: In case the bacteria have the ability to signal to others the existence of a favorable or poisonous environment, they will tend to swarm together in the direction of nutrients. The cell to cell attraction or rejection is modeled by adding to the cost function $J(i, j, k, l)$ computed for a specific bacterium, components computed as function of the status of all the other bacteria in the colony.

- *Reproduction*: All bacteria reach the reproduction state after a number of chemotactic steps. The healthy state is computed for all bacteria and it may be expressed as the total quantity of accumulated nutrients or simply by the value of the cost function in the current position. The least healthy bacteria die while and to keep constant the size of the colony, an equal number of healthier bacteria split into two bacteria without mutation.
- *Elimination and Dispersal*: After a number of reproduction steps, some bacteria are dispersed into the environment (moved in a random position) with a specified probability, without taking into account their healthy state.

BFOA starts with a colony of S bacteria placed in randomly generated positions. The evolutionary process goes through N_{ed} elimination/dispersal steps, each of these consists of N_{re} reproduction steps. Each reproduction step consists of N_c chemotactic steps. In each chemotactic step a bacterium may do at most N_s swimming steps if the value of the cost function decreases. The position in which a bacterium has the greatest healthy status is the solution of the optimization problem. In case of image registration, the size of the search space is equal to the number of parameters of the geometric transform and as healthy status is used the value of a measure that evaluates the similarity between the transformed source image and the model image.

2.2 Parallel Version of BFO Algorithm

A closer look at BFOA reveals that it contains 4 nested loops: elimination/dispersal, reproduction and chemotaxis for each bacterium in the colony. The body of the inner loop is executed $N_{ed} \times N_{re} \times N_C \times S$ times, which may be a fairly large number. In the examples presented in the next sections, it is executed 256000 times, but the cost function evaluation is performed about 600000 times due to the fact that each bacterium may perform more swim steps in a single chemotactic step.

We propose a parallelization based on the shared memory model that is suitable for multi-core processor based systems. It must be noticed that in this case the number of available processors is reduced (2, 4 or 8). An excessive tasks partitioning obviously leads to poor performances due to the large number of synchronization operations.

If we consider to not use the attractant/repellant effect in the optimization algorithm, then the calculations performed for each individual bacterium in the inner loop are independent excepting the test in which the best value of the cost function is checked. So, we can execute in parallel a chemotactic step for all bacteria, taking care to not simultaneously call the function to check for the best value of the cost function.

3 Pixel Based Image Registration

The proposed IR procedures use the Normalized Mutual Information and Normalized Cross Correlation as measures to evaluate the quality of the registration process.

Our study approaches the *rigid body image registration*, which initially determines global alignment, followed by local elastic registration. Let \mathbf{T} denote the spatial transformation that maps features or coordinates (spatial locations) from one image or coordinate space to another image or coordinate space. Let \mathbf{p}_A and \mathbf{p}_B denote coordinate points (pixel locations) in images A and B , respectively. The image registration problem is to determine T so that the mapping $\mathbf{T} : \mathbf{p}_A \rightarrow \mathbf{p}_B \Leftrightarrow \mathbf{T}(\mathbf{p}_A) = \mathbf{p}_B$ results in the "best" alignment of A and B . For 3-D rigid body registration, the mapping of coordinates $\mathbf{p} = [x, y, z]^T$ into $\mathbf{p}' = [x', y', z']^T$ can be formulated as a matrix multiplication in homogeneous coordinates, as shown in equation (2) in an explicit manner. That is, the goal of the optimization is to determine the parameters $t_x, t_y, t_z, \alpha, \beta$, and

γ in (2). Usually, optimization in image registration means to maximize similarity. Similarity metric values, as functions of transformation parameters, refer to the *objective function*, denoted as $f(\mathbf{x})$. Alternatively, one may formulate the image registration as a minimization problem and, thus, the goal is to minimize $-f(\mathbf{x})$. Although there is yet no proof for its optimality, because of its robustness (usually it attains its maximum at correct alignment) and good results in previous works, normalized mutual information was selected as the similarity measure in our study. Moreover, it is still generally non-smooth and prone to local optima. For this reason, global optimization approaches are preferred.

$$\begin{bmatrix} p' \\ 1 \end{bmatrix} = \mathbf{T} \begin{bmatrix} p \\ 1 \end{bmatrix} \Leftrightarrow \begin{bmatrix} x' \\ y' \\ z' \\ 1 \end{bmatrix} = \begin{bmatrix} \cos \beta \cos \gamma & \cos \alpha \sin \gamma + \sin \alpha \sin \beta \cos \gamma & \sin \alpha \sin \gamma - \cos \alpha \sin \beta \cos \gamma & t_x \\ -\cos \beta \sin \gamma & \cos \alpha \cos \gamma - \sin \alpha \sin \beta \sin \gamma & \sin \alpha \cos \gamma - \cos \alpha \sin \beta \sin \gamma & t_y \\ \sin \beta & -\sin \alpha \cos \beta & \cos \alpha \cos \beta & t_z \\ 0 & 0 & 0 & 1 \end{bmatrix} \begin{bmatrix} x \\ y \\ z \\ 1 \end{bmatrix} \quad (2)$$

3.1 Normalized Mutual Information

Mutual Information (*MI*) and Normalized Mutual Information (*NMI*) evaluate the relative independence of two images and do not depend on the specific dynamic range or intensity scaling of the images [1], [10]:

$$MI(A, B) = H(A) + H(B) - H(A, B) \quad (3)$$

$$NMI(A, B) = (H(A) + H(B)) / H(A, B), \quad (4)$$

where $H(A)$, $H(B)$ are the image entropies and $H(A, B)$ is the joint entropy of the two images. High values of mutual information indicate high dependence between images. Because the goal of the optimization algorithms is to minimize a cost function, the value of $(-1) * NMI$ will be used to evaluate the quality of a certain solution. In the cost function evaluation, the geometric transform corresponding to the current solution is applied to the source image and then the *NMI* value is computed for the model image and the transformed source image. The area based IR implementations are time consuming because each cost evaluation requires a geometric transform to be applied and also image and matrix operations to compute *NMI*.

3.2 Normalized Cross Correlation

Cross correlation is used for estimating the degree to which two series are correlated. One of the most encountered applications of the normalized cross correlation is to determine the position of a template sub-image B in a source image A . The normalized cross correlation (*NCC*) is computed by

$$NCC(i, j) = \frac{\sum_{\bar{i}} \sum_{\bar{j}} A(i + \bar{i}, j + \bar{j}) \cdot B(\bar{i}, \bar{j})}{\sqrt{\sum_{\bar{i}} \sum_{\bar{j}} B(\bar{i}, \bar{j})^2} \cdot \sqrt{\sum_{\bar{i}} \sum_{\bar{j}} A(i + \bar{i}, j + \bar{j})^2}}. \quad (5)$$

The problem is to determine the position of a given pattern in a two dimensional image f . Let $f(x, y)$ denote the intensity value of the image f of size $M_x \times M_y$ at the point (x, y) , $x \in \{0, \dots, M_x - 1\}$, $y \in \{0, \dots, M_y - 1\}$. The pattern is represented by a given template t of size $N_x \times N_y$. A common way to calculate the position (u_{pos}, v_{pos}) of the pattern in the image f is to evaluate the normalized cross correlation value γ at each point (u, v) for f and template

t , which has been shifted by u steps in the x direction and by v steps in the y direction. The following equation gives a basic definition for the normalized cross correlation coefficient

$$\gamma = \frac{\sum_{x,y}(f(x,y) - \overline{f_{u,v}})(t(x-u, y-v) - \bar{t})}{\sqrt{\sum_{x,y}(f(x,y) - \overline{f_{u,v}})^2 \sum_{x,y}(t(x-u, y-v) - \bar{t})^2}}, \quad (6)$$

where $(\overline{f_{u,v}})$ denotes the mean value of $f(x,y)$ within the area of the template t shifted to (u, v) , which is computed by:

$$(\overline{f_{u,v}}) = \frac{1}{N_x N_y} \sum_{x=u}^{u+N_x-1} \sum_{y=v}^{v+N_y-1} f(x,y). \quad (7)$$

With similar notation, \bar{t} is the mean value of the template t . The denominator in (6) is the variance of the zero mean image function $f(x,y) - \overline{f_{u,v}}$ and the shifted zero mean template function $t(x-u, y-v) - \bar{t}$. Due to this normalization, $\gamma(u,v)$ is independent to changes in brightness or contrast of the image, which are related to the mean value and the standard deviation.

4 Experiments and Results

The BFOA based image registration procedure was tested on a large set of DICOM medical images from a database at the address <http://www.osirix-viewer.com/datasets/> [39]. In Figure 1 below, information about some test images are shown.


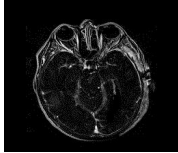

Image	Description:
	File : img_1.tif Size : 256 × 256 × 8b Name : PETCETIX Modality : PET-CT Description: Whole body FDG PET-CT study in a patient with abdominal lymphoma.
	File: img_2.tif Size: 256 x 256 x 8b Name: BRAINIX Modality: MR Description: Brain tumor.
	File: img_3.tif Size: 256 x 256 x 8b Name: WRIX Modality: MRI Description: Scaphoid fracture. T1 / STIR fusion.

Figure 1: Test images used in the experiment

In the experiment, 4 images were used: img_1 , img_2 , $\text{img_2}_{\text{HistEq}}$ (that was obtained by applying the histogram equalization to img_2 having low contrast), and img_3 .

The source images were obtained by applying a rotation (angle $\theta = 10^\circ$) against the rotation center ($c_x = -20$ and $c_y = 20$) followed by an isotropic scaling ($scale = 1.2$). The transform matrix is:

$$T = \begin{bmatrix} \alpha & \beta & (1 - \alpha)c_x - \beta c_y \\ -\beta & \alpha & \beta c_x + (1 - \alpha)c_y \\ 0 & 0 & 1 \end{bmatrix} \quad (8)$$

where $\alpha = \text{scale} \cdot \cos \theta$ and $\beta = \text{scale} \cdot \sin \theta$. The actual value of the transform matrix is

$$T = \begin{bmatrix} 1.1818 & 0.2084 & -0.5322 \\ -0.2084 & 1.1818 & -7.8029 \\ 0 & 0 & 1 \end{bmatrix} \quad (9)$$

The inverse transform matrix is $T^{-1} = \begin{bmatrix} 0.8207 & -1.1477 & -0.6924 \\ 1.1447 & 0.8207 & 6.4807 \\ 0 & 0 & 1 \end{bmatrix}$ that corresponds to an affine transform with the following parameters: $\theta' = -10^\circ$, $c'_x = -20$, $c'_y = 20$ and $\text{scale}' = 0.8333$. The search space for the optimization problem is R^4 .

The BFO parameters values used in the experiment are:

Colony size, $S = 400$; Number of chemotactic steps, $N_c = 20$; Maximum number of swim steps, $N_s = 10$; Number of reproduction steps, $N_{re} = 16$; Number of elimination/dispersal steps, $N_{ed} = 2$; Probability of dispersal, $P_{ed} = 0.25$; Length of the move $\text{step} = 0.001$.

As it can be observed in Figure 1 the test images have the same size but are different in terms of contrast. It was expected that the image contrast affects the quality of the registration process, and this assumption was found to be true.

In vision, *contrast* is the difference in luminance that makes an object distinguishable. The test images we used in this paper were not analyzed for their content (i.e., it is a context-free registration), so the contrast and his evaluation was performed by means of the histogram of the images.

Root *mean square contrast* is computed as standard deviation of pixel values. It does not depend on the spatial frequency or spatial distribution in the image.

$$\text{Contrast}_{RMS} = \sqrt{\frac{1}{MN} \sum_{i=1}^N \sum_{j=1}^M (I(i, j) - I_{avg})^2}, \quad (10)$$

where M, N are the image dimensions, $I(i, j)$ is the image pixel at (i, j) coordinates and I_{avg} is the average of pixel values in image I .

Visibility (Michelson contrast) is represented by formula

$$\text{Contrast}_{Michelson} = \frac{I_{\max} - I_{\min}}{I_{\max} + I_{\min}}, \quad (11)$$

where I_{\min} and I_{\max} are the lowest and highest pixel values in image I , respectively.

Contrast values computed for the tested model images are described in Table 1.

Table 1: Contrast values computed for the test images

Image	Gray values			Contrast	
	min	max	average	Michelson	RMS
img_1	0	255	56.7	1.0	0.27
img_2	0	146	6.0	1.0	0.05
img_2_HistEq	0	255	74.7	1.0	0.35
img_3	19	238	39.7	0.85	0.15

For image_img_2.tif with initial low contrast a histogram equalization procedure was performed and image named img_2_HistEq was obtained. The source images were obtained by applying the affine transform specified above followed by salt-and-pepper and Gaussian noise alteration.

The Signal-To-Noise Ratio was computed using the formula below and is shown in Table 2.

$$SNR = 10 \log \frac{\sum_{i=1}^N \sum_{j=1}^M I(i, j)^2}{\sum_{i=1}^N \sum_{j=1}^M (I(i, j) - I_{noise}(i, j))^2} dB, \quad (12)$$

Table 2: Signal-to-Noise Ratio (SNR) values for testimages with noise

Image	Gray values			Contrast	
	min	max	average	Michelson	RMS
img_1	0	255	56.7	1.0	0.27
img_2	0	146	6.0	1.0	0.05
img_2_HistEq	0	255	74.7	1.0	0.35
img_3	19	238	39.7	0.85	0.15

The registered images for test image img_1 are shown in Figure 2.

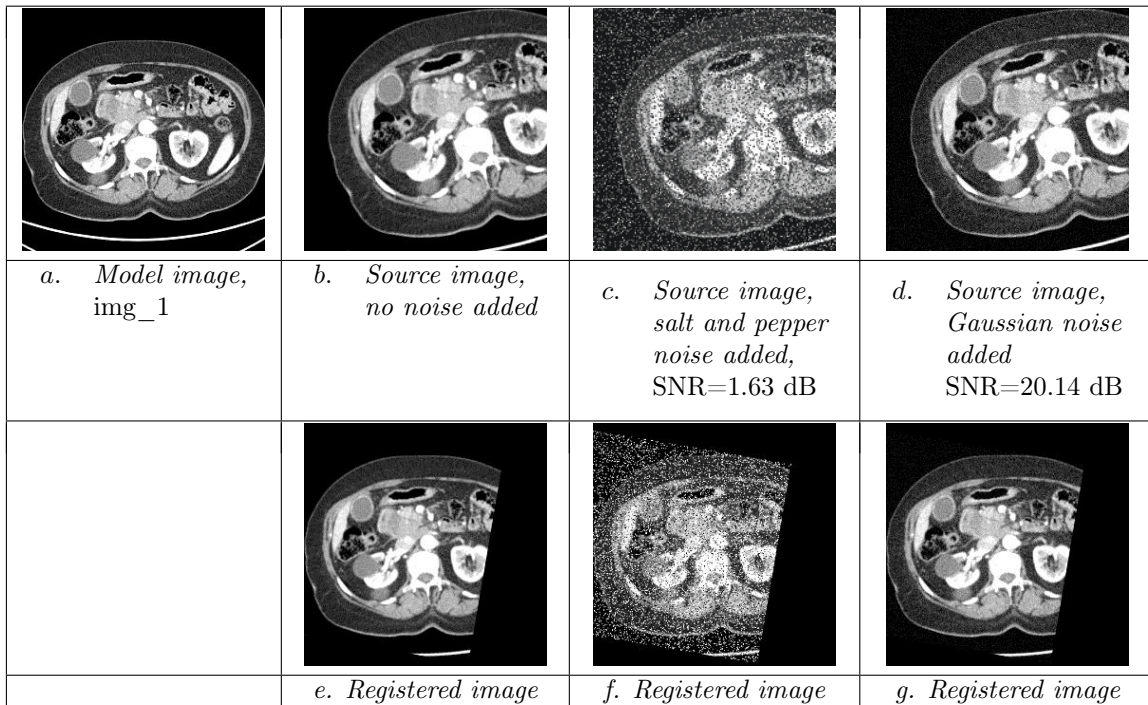


Figure 2: Registered images for test image img_1

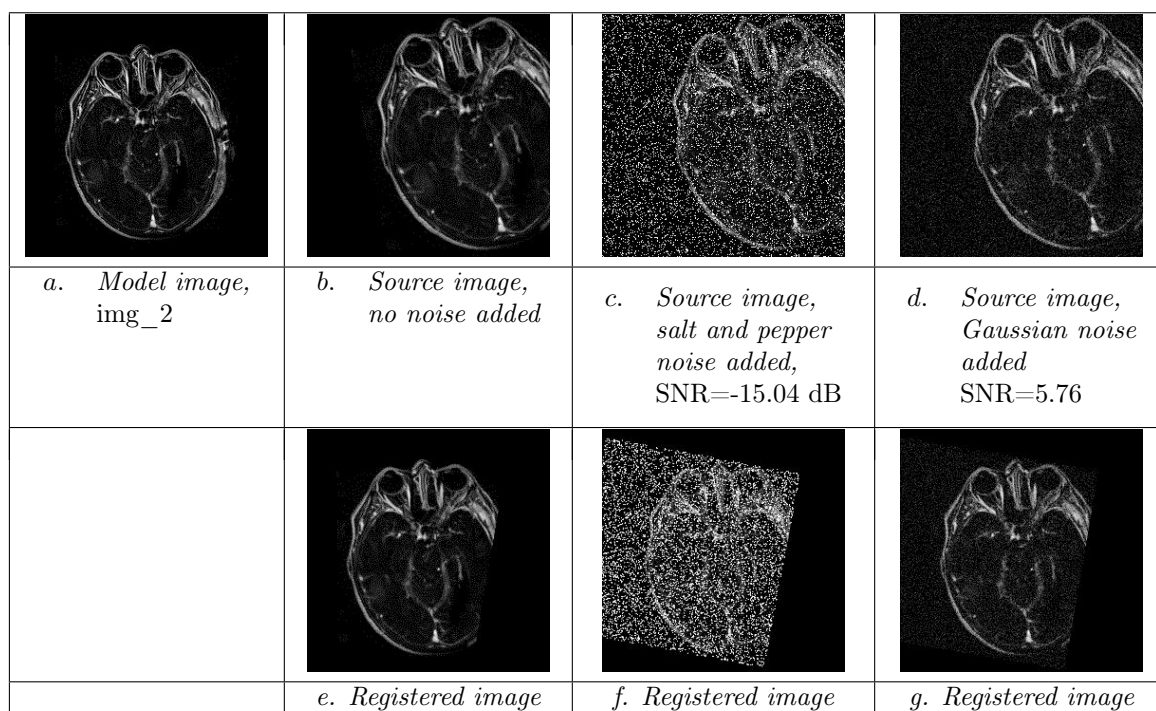
In Table 3, the columns NMI/Expected and NCC/Expected contain respectively the values of Mutual Information and Normalized Cross Correlation computed for the model image and the image obtained by applying the inverse affine transform on the source images. The NMI/Computed and NCC/Computed contain respectively the Mutual Information and Normalized Cross Correlation computed for the model image and the registered image obtained by applying the approximated affine transform. The first 3 rows in Table 3 contain the values obtained using MI as similarity measure while the last 3 rows contain the results obtained by using NCC as similarity measure in the registration evaluation.

Table 3: Image registration results obtained for test image *img_1*

Similarity	Added Noise, SNR	NMI		NCC		Computed inverse transform			
		Expected	Computed	Expected	Computed	c_x	c_y	θ	scale
NMI	-	1.255	1.215	0.896	0.893	-24.963	20.101	-9.708	0.834
	S&P, 1.63 dB	1.129	1.119	0.782	0.780	-25.270	19.444	-9.657	0.834
	Gaussian, 20.14 dB	1.199	1.188	0.894	0.892	-23.730	19.062	-9.783	0.835
NCC	-	1.255	1.205	0.896	0.892	-26.209	19.702	-9.625	0.835
	S&P, 1.63 dB	1.128	1.119	0.784	0.783	-25.773	20.007	-9.630	0.834
	Gaussian, 20.14 dB	1.199	1.182	0.894	0.891	-25.538	21.529	-9.597	0.834

In the case of the image drawn in Figure 2, it must be noticed that in all cases the value of the similarity measure computed for the registered image does not exceed the expected value. This happens because the image histogram is uniform (the gray levels are more uniformly distributed in the image), even if there does exist a considerable number of black pixels. Accordingly, the results obtained using the two similarity measures are quite similar.

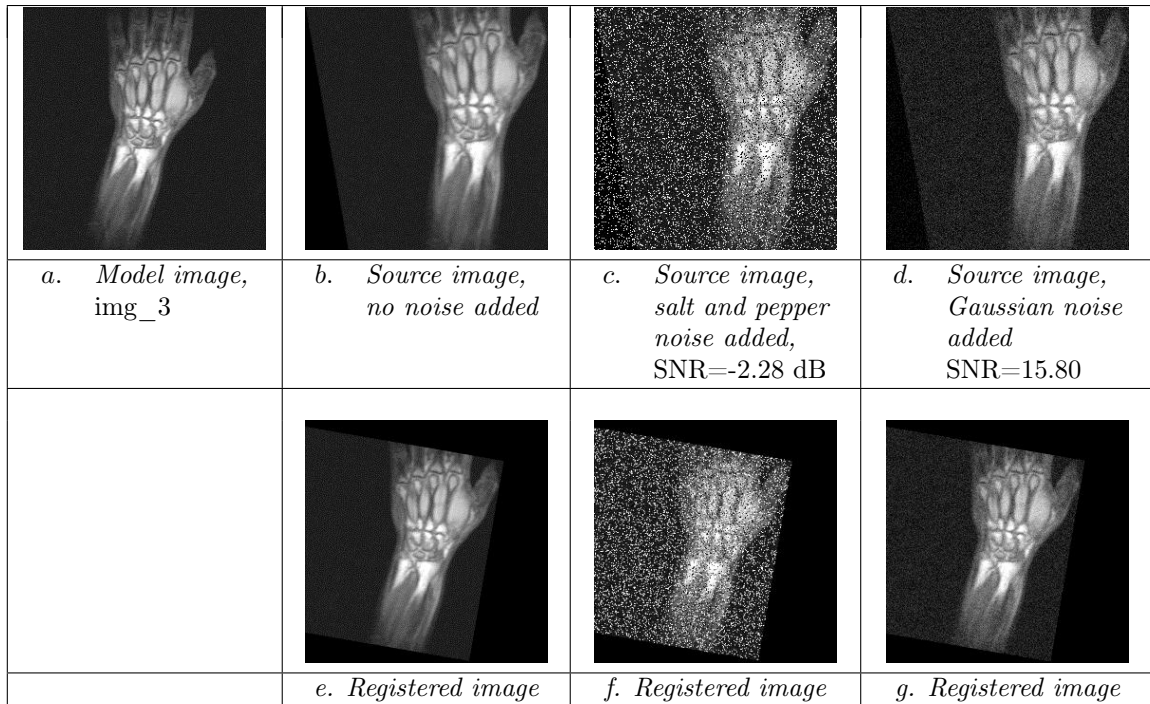
Similarly, registered images for test image *img_2* are depicted in Figure 3.

Figure 3: Registered images for test image *img_2*

In the case of test image *img_2*, even if the image has a low contrast, the IR result is also good. The image contrast is $Contrast_{RMS} = 0.05$ (a very low value) and in all cases the similarity measure error is less than $1/1000$, so the proposed BFOA-based IR method works well in case of low contrast images. Moreover, for very noisy images (SNR as low as $-15.04dB$) this method also works very well, as shown in Figures 3 (*f, g*).

Table 4: Image registration results obtained for test image *img_2*

Similarity	Added Noise, SNR	NMI		NCC		Computed inverse transform			
		Expected	Computed	Expected	Computed	c_x	c_y	θ	scale
NMI	-	1.226	1.187	0.923	0.916	-25.026	19.450	-9.684	0.835
	S&P, -15.04 dB	1.110	1.101	0.849	0.845	-24.837	20.368	-9.668	0.834
	Gaussian, 5.76	1.198	1.174	0.922	0.917	-24.008	18.941	-9.771	0.835
NCC	-	1.226	1.176	0.923	0.914	-26.053	19.905	-9.607	0.836
	S&P, -15.04 dB	1.111	1.101	0.850	0.846	-24.638	21.124	-9.677	0.834
	Gaussian, 5.76	1.198	1.196	0.922	0.922	-20.056	19.796	-9.991	0.834

Figure 4: Registered images for test image *img_3*Table 5: Image registration results obtained for test image *img_3*

Similarity	Added Noise, SNR	NMI		NCC		Computed inverse transform			
		Expected	Computed	Expected	Computed	c_x	c_y	θ	scale
NMI	-	1.351	1.302	0.854	0.954	-22.549	18.654	-9.873	0.835
	S&P, -2.28	1.122	1.102	0.772	0.773	-25.759	18.014	-9.633	0.837
	Gaussian, 15.80	1.159	1.155	0.949	0.949	-25.641	16.334	-9.750	0.838
NCC	-	1.351	1.225	0.954	0.955	-26.621	15.157	-9.677	0.840
	S&P, -2.28	1.123	1.084	0.773	0.778	-26.407	-37.414	-10.042	0.886
	Gaussian, 15.80	1.159	1.152	0.949	0.949	-26.876	13.791	-9.657	0.842

In case of the test image *img₃* (Table 5), it must be noticed that in all experimental situations the computed NCC value is very slightly greater than the expected value. This may be explained by: (1) the low contrast of model and source images, (2) the images have a high portion of dark background and (3) the black areas inserted (as a necessity, from experimental reasons) in the transformed and registered images after the affine transforms application. But also in these conditions the values of MI seem to be more relevant and give a real evaluation of the registration

process.

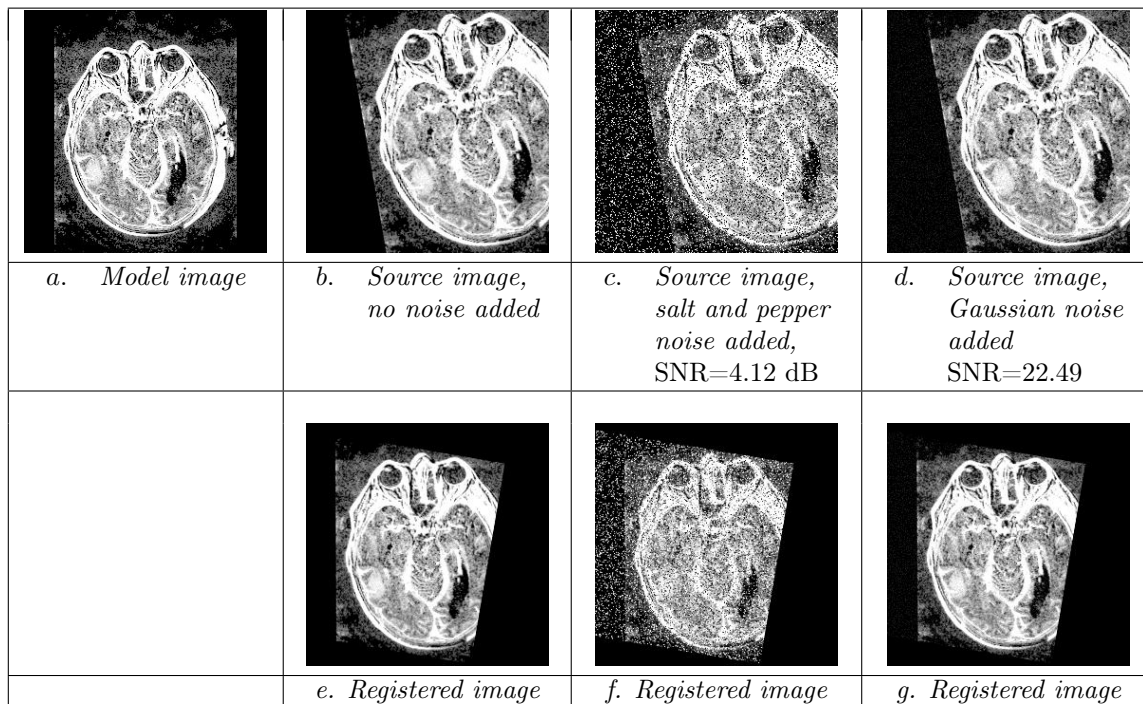


Figure 5: Registered images for test image `img_2_HistEq`

The proposed IR procedure was also applied to the low contrast image `img_2`, processed by applying the histogram equalization (Figure 5). In this way the contrast value was increased from 0.05 to 0.35. It must be noticed that in this case the registration results are similar to the case of the original image, `img_2` (Table 6).

Table 6: Image registration results obtained for test image `img_2_HistEq`

		NMI		NCC		Computed inverse transform			
Similarity	Added Noise, SNR	Expected	Computed	Expected	Computed	c_x	c_y	θ	scale
NMI	-	1.226	1.181	0.923	0.915	-24.543	17.356	-9.710	0.837
	S&P, 4.12 dB	1.110	1.096	0.849	0.842	-26.152	18.808	-9.604	0.836
	Gaussian, 22.49 dB	1.198	1.166	0.922	0.914	-25.166	21.608	-9.624	0.833
NCC	-	1.226	1.169	0.923	0.912	-26.339	18.247	-9.615	0.837
	S&P, 4.12 dB	1.111	1.109	0.850	0.850	-18.283	19.322	10.118	0.834
	Gaussian, 22.49 dB	1.198	1.175	0.922	0.918	-24.136	20.753	-9.718	0.834

4.1 Execution Time and Parallel Approach of the Algorithm

The following tables contain for each test image the execution time in seconds, the number of cost function evaluations for sequential and parallel executions and also the *parallel efficiency* (Eff). The most common evaluation of parallel algorithms is performed using the parallel efficiency $Eff = \frac{t_s}{t_p \times n}$, where t_s is the time used by the sequential version of the algorithm, t_p is the processing time for the parallel version and n is the number of used processors [38].

When comparing these values, the following issues must be considered:

- The parallel implementation was evaluated on Intel Core i5 3.10 GHz processor, with 4 cores. The system has 4 GB RAM and uses Windows 7 (64 bits) as operating system. The application was compiled as a 32 bits application;

- The execution times have to be considered as approximations, because the application was executed in Windows OS without obtaining the exclusive access of processor. The processor allocation during parallel execution was made by the operating system;
- In all executions of BFOA, the random number string was the same (the generator was initialized using the same value).

In Table 7 and Table 8 below the execution time (in seconds), the number of cost function evaluations and parallel efficiency are presented.

Table 7: Parallel efficiency obtained for images img_1 and img_3

Image		img_1					img_3				
		Sequential		Parallel			Sequential		Parallel		
Similarity	Added Noise	Time (s)	#cost	Time (s)	#cost	Eff	Time (s)	#cost	Time (s)	#cost	Eff
NMI	-	839.769	570692	244.220	568823	0.86	694.267	586892	218.744	589716	0.79
	S&P	859.737	535249	248.010	532361	0.87	718.868	535803	220.960	532431	0.81
	Gaussian	838.271	565463	244.094	567932	0.86	695.468	573242	219.478	572184	0.79
NCC	-	2173.749	653157	647.888	654266	0.84	2312.044	686083	685.157	686872	0.84
	S&P	2032.006	606303	602.491	609533	0.84	1927.860	571561	580.043	575190	0.83
	Gaussian	2061.705	650318	646.531	653771	0.80	2269.206	671327	687.808	674931	0.82

Table 8: Parallel efficiency obtained for images img_2 and img_2_HistEq

Image		img_2					img_2_HistEq				
		Sequential		Parallel			Sequential		Parallel		
Similarity	Added Noise	Time (s)	#cost	Time (s)	#cost	Eff	Time (s)	#cost	Time (s)	#cost	Eff
NMI	-	685.63	567856	218.67	569872	0.78	691.07	567856	221.71	570865	0.78
	S&P	667.93	537816	210.76	539742	0.79	671.09	537816	210.49	535776	0.80
	Gaussian	682.24	569109	216.31	568918	0.79	689.23	569109	218.71	568197	0.79
NCC	-	2295.84	678710	665.08	673911	0.86	2306.49	678710	674.81	677368	0.85
	S&P	2110.49	623178	617.76	624415	0.85	2120.18	623178	617.97	625897	0.86
	Gaussian	2296.54	676781	682.82	680036	0.84	2307.30	676781	680.80	675274	0.85

Also, Figures 6 and 7 show parallel versus sequential execution time for img_2 and img_2_HistEq respectively, for clean and different added noise.

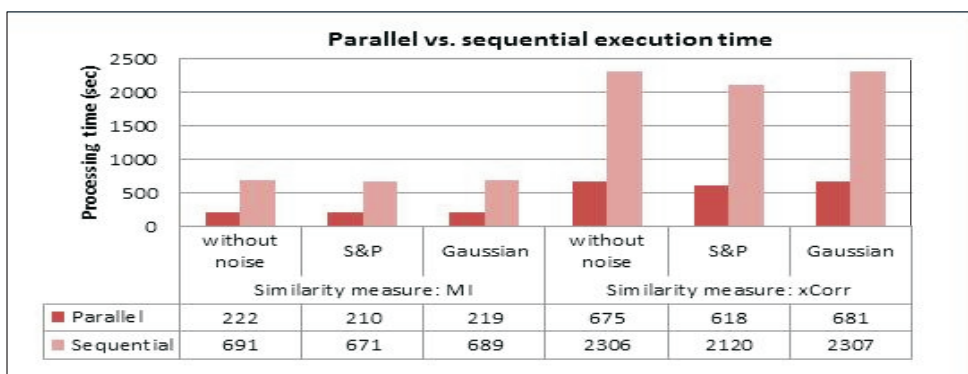


Figure 6: Parallel and sequential execution time in case of image img_2_HistEq

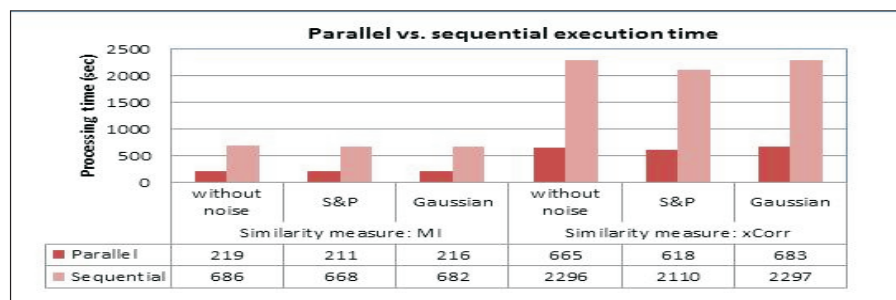


Figure 7: Parallel and sequential execution time in case of image `img_2`

As is depicted in Table 7 and Table 8, the parallel efficiency value is between 0.78 and 0.86. Higher values of efficiency are obtained for longer tasks, when normalized cross correlation is used for image similarity evaluation. It must be noticed that in this case, the parallel version execution time is similar to the sequential version execution time when NMI is used for similarity evaluation. Considering that also the registration precision is higher in case of NMI usage, it can be concluded that NMI is recommended as evaluation measure. The obtained parallel efficiency value is high, considering the time required for synchronization tasks and critical sections which cannot be parallelized. It must be noticed that in case of images `img_2` and `img_2_HistEq`, for the sequential image registration, the cost function is called the same number of times. The execution time is different because in Windows operating system the processor is also used for other tasks. In case of parallel image registration, the number of cost function evaluation is different for the different allocation of the processor cores. Figures 6 and 7 show processing time for different added noise and the two similarity measures considered, for sequential and parallel versions of the proposed algorithm, when registering images `img_2_HistEq` and `img_2`, respectively.

5 Conclusions

This study proved the feasibility of rigid and mono-modal image registration by using a new optimization approach - Bacterial Foraging Optimization Algorithm (BFOA), a bio-inspired technique that belongs to the large family of evolutionary computing and metaheuristic methods. As similarity measures between two images performing registration process, we used the normalized mutual information and normalized cross correlation which had to be optimized by BFOA. The obtained results are encouraging, i.e. the accuracy of registration process as high even in the case of noisy images, with very low signal-to-noise ratios. In this way our method might be considered as a robust registration technique. Yet, the maximum expected value of the IR evaluation measure was not reached because when processing images from the used database two technical details have limited the overall registration:

- after the affine transform applied to obtain the source image and inverse transform is applied to obtain the registered image, some black areas are inserted in some images due to geometrical experimental reasons;
- the pixels values are changed because during the direct and inverse affine transform the pixels values are approximated using interpolation methods. In this experiment the bilinear interpolation is used.

Concerning the possibility to accelerate the execution time of the registration process, it is noteworthy that the proposed algorithm is suited to parallelization, as shown above. In this respect runtimes at least 3 times lower of the parallel version than of sequential approach were obtained, so the parameter named "speedup" equals 3. When computing parallel efficiency, it is worth mentioning that values of 0.78–0.86 were obtained when using the Intel Core i5 processor (4 cores), that meaning a good efficiency of the parallel approach.

Bibliography

- [1] Cordon, O.; Damas, S.; Santamaria, J. (2006); Feature-based Image Registration by Means of the CHC Evolutionary Algorithm, *Image and Vision Computing*, 24(5): 525-533.
- [2] Gonzales, R.C.; Woods, R.E. (2002); *Digital Image Processing* (2nd ed.), Prentice Hall, New Jersey.
- [3] Pratt, W.K. (2001); *Digital Image Processing*, John Wiley & Sons, New York.
- [4] Rangayyan, R.M. (2005); *Biomedical Image Analysis*, CRC Press, Boca Raton, 2005.
- [5] Alterovitz, R., et al. (2006); Registration of MR Prostate Images with Biomechanical Modeling and Nonlinear Parameter Estimation, *Medical Physics*, 33(2): 446-454.
- [6] Cooper, J. (2003); Optical Flow for Validating Medical Image Registration, *Proc. of the 9th IASTED Int. Conference on Signal and Image Processing*, IASTED/ACTA Press: 502-506.
- [7] He, R.; Narayana, P.A. (2002); Global Optimization of Mutual Information: Application to Three Dimensional Retrospective Registration of Magnetic Resonance Images, *Computerized Medical Imaging and Graphics*, 26(4): 277-292.
- [8] Hill, D.; Studholme, C.; Hawkes, D. (1994); Voxel Similarity Measures for Automated Image Registration, *Proceedings of the Third SPIE Conference on Visualization in Biomedical Computing*: 205-216.
- [9] Lavavelly, W.C.; Scarfone, C. et al. (2004); Phantom Validation of Co-Registration of PET and CT for Image-Guided Radiotherapy, *Medical Physics*, 31(5): 1083-92.
- [10] Levin, D.N.; Pelizzari, C.A. et al. (1988); Retrospective Geometric Correlation of MR, CT, and PET Images, *Radiology*, 169(3): 817-823.
- [11] Lee, H.; Hong, H. (2006); Robust Surface Registration for Brain PET-CT Fusion, *Medical Imaging 2006: Visualization, Image-Guided Procedures, and Display*, Ed. by Cleary, Kevin R.; Galloway, Robert L., Jr., *Proceedings of the SPIE*, 6141: 684-693.
- [12] Maintz, B.A.; van den Elsen, P.A.; Viergever, M.A. (1996); Registration of SPECT and MR Brain Images Using a Fuzzy Surface, in Loew, M.H. and Hanson, K.M. (eds), *Medical Imaging: Image processing*, Bellingham, WA. SPIE, 2710: 821-829.
- [13] Maintz, B.A.; Viergever, M.A. (1998); *A Survey of Medical Image Registration*, *Medical Image Analysis*, Oxford University Press, 2(1): 1-37.
- [14] Pluim, J.P.; Maintz, J.B.A.; Viergever, M.A. (2003); Mutual Information-based Registration of Medical Images: A Survey, *IEEE Transactions on Medical Imaging*, 22(8): 986-1004.
- [15] Pietrzyk, U., Herholz, K. et al., (1996); Clinical Applications of Registration and Fusion of Multimodality Brain Images from PET, SPECT, CT, and MRI, *European Journal of Radiology*, 21: 174-182.
- [16] Chen, Qin-Sheng (1993); *Image Registration and Its Applications in Medical Imaging*, PhD thesis, Vrije Universiteit Brussel.
- [17] Zibaeifard, M.; Rahmati, M. (2001); An Improved Multi-stage Method for Medical Image Registration Based on Mutual Information, *Proceedings of the 8-th International Conference on Computer Vision*: 718-725.

-
- [18] Xuan, J.; Wang, Y. et al. (2006); Nonrigid Medical Image Registration by Finite-element Deformable Sheet-curve Models, *Int. Journal of Biomedical Imaging*, 2006, Article ID 73430: 1-9, Hindawi Publishing Corporation.
- [19] Zitova, B., Flusser, J. (2003); Image Registration Methods: A Survey, *Image and Vision Computing*, 21, Elsevier, 977-1000.
- [20] Alpert, N.M.; Bradshaw, J.F.; Kennedy, D.; Correia, J.A. (1990); The Principal Axis Transformation – A Method for Image Registration, *Journal of Nuclear Medicine*, 31, 1717-1722.
- [21] Wahl, R.L.; Quint, L.E.; et al. (1993); "Anametabolic" Tumor Imaging: Fusion of FDG PET with CT or MRI to Localize Foci of Increased Activity. *Journal of Nuclear Medicine*, 34: 1190-1197.
- [22] Maguire, G.Q. Noz, M. et al. (1991); Graphics Applied to Medical Image Registration. *IEEE Computer Graphics and Applications*, 11(2): 20-28.
- [23] Back, T.; Fogel, D.B.; Michalewicz, Z. (Eds.) (1997); *Handbook of Evolutionary Computation*, IOP, Bristol, UK; Oxford University Press, Oxford, UK.
- [24] Fitzpatrick, J.M.; Grefenstette, J.J.; Van Gucht, D. (1984); Image Registration by Genetic Search, *Proc. of the IEEE Southeast Conference*, Louisville, USA, 460-464.
- [25] Chow, C. K.; Tsui, H.T.; Lee, T. (2004); Surface Registration Using a Dynamic Genetic Algorithm, *Pattern Recognition*, 37(1): 105-117.
- [26] Cordon, O.; Damas, S.; Santamaria, J. (2007); A Practical Review on the Applicability of Different Evolutionary Algorithms to 3D Feature-based Image Registration, in *Genetic and Evolutionary Computation for Image Processing and Analysis*, Eds.: S. Cagnoni, E. Lutton, G. Olague, Hindawi Publishing Corporation, 241-264.
- [27] Etienne, E.K.; Nachtgeael, M. (2000) (eds.). *Fuzzy Techniques in Image Processing*, Physica-Verlag, N.Y.
- [28] Reyes-Sierra, M.; Coello C.A. (2006); Multi-objective Particle Swarm Optimizers: A Survey of the State-of-the-art, *International Journal of Computational Intelligence Research*, 2(3): 287-308.
- [29] Rouet, J.-M.; Jacq, J.-J.; Roux, C. (2000); Genetic Algorithms for a Robust 3-D MR-CT Registration, *IEEE Trans. on Information Technology in Biomedicine*, 4(2): 126-136.
- [30] Wachowiak, M. P.; Smolíková, R. et al. (2004); An Approach to Multimodal Biomedical Image Registration Utilizing Particle Swarm Optimization, *IEEE Transactions on Evolutionary Computation*, 8(3): 289-301.
- [31] Passino, K.M. (2002); Biomimicry of Bacterial Foraging for Distributed Optimization and Control, *IEEE Control Systems Magazine*, 52-67.
- [32] Liu, Y.; Passino, K.M. (2002); Biomimicry of Social Foraging Bacteria for Distributed Optimization: Models, Principles, and Emergent Behaviors, *Journal of Optimization Theory and Applications*, 115(3): 603-628.
- [33] Verma, O. P.; Hanmandlu, M.; Kumar, P.; Chhabra, S.; Jindal, A. (2011); A Novel Bacterial Foraging Technique for Edge Detection, *Pattern Recognition Letters*, Elsevier, 32: 1187-1196.

-
- [34] N. Sanyal, A. Chatterjee, S. Munshi (2011); "An Adaptive Bacterial Foraging Algorithm for Fuzzy Entropy Based Image Segmentation", *Expert Systems with Applications*, Elsevier, 38: 15489-15498.
- [35] Sathya, P.D.; Kayalvizhi, R. (2011); Modified Bacterial Foraging Algorithm Based Multi-level Thresholding for Image Segmentation, *Engineering Applications of Artificial Intelligence*, Elsevier, 24: 595-615.
- [36] Yudong, Z.; Lenan, W. (2008); Multi-resolution Rigid Image Registration Using Bacterial Multiple Colony Chemotaxis, *5th Int. Conf. on Visual Information Engineering*, VIE 2008, 528-532.
- [37] Bejinariu, S. I.; Costin, H., Rotaru, F.; Niță, C.; Luca, R.; Lazăr, C. (2014); Parallel Processing and Bioinspired Computing for Biomedical Image Registration, *The Computer Science Journal of Moldova*, 22(2): 253-277.
- [38] Campbell, C.; Miller, A. (2012); *Parallel Programming with Microsoft Visual C++*, Microsoft Corporation.
- [39] DICOM Sample Image Sets (<http://www.osirix-viewer.com/datasets/>), accessed on 1.09.2014